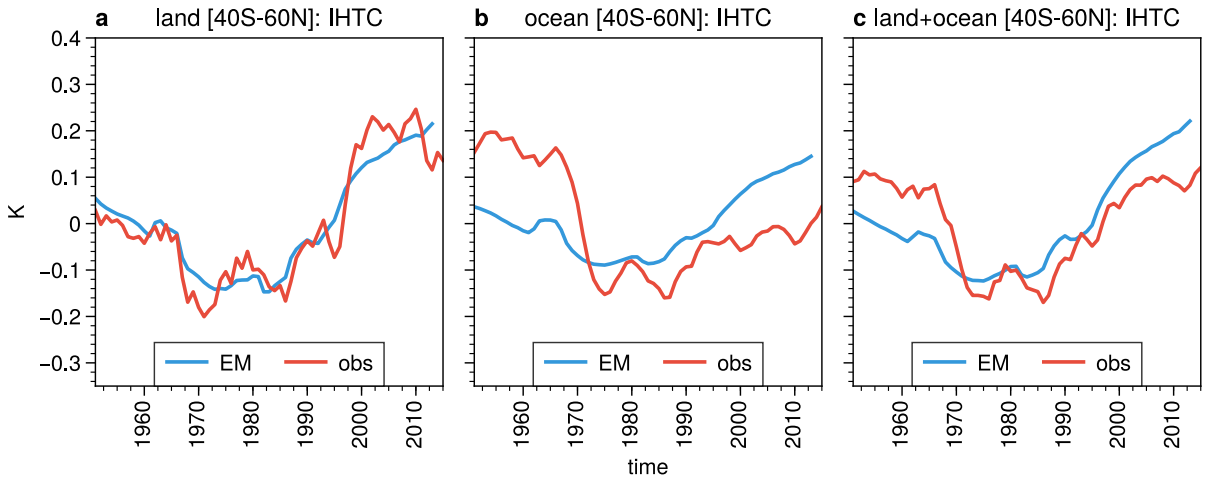

Extended Data Fig. 1 Interhemispheric surface temperature contrast in the model and observation. a, land surface temperature contrast. **b,** SST. **c,** land and ocean surface temperature contrast. A 7-yr running mean has been applied to time series for presentation.

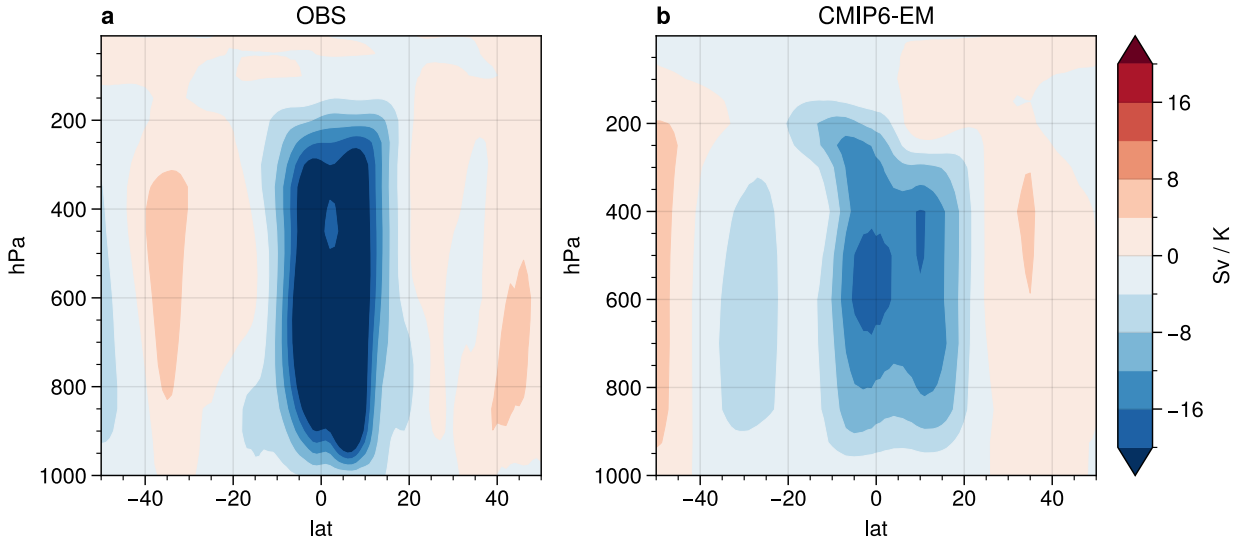

Extended Data Fig. 2 Regression of overturning mass streamfunction on the IHTC in observation (a) and model (b). 1Sv = 10^9 kg/s. Positive values indicate clockwise overturning circulation.

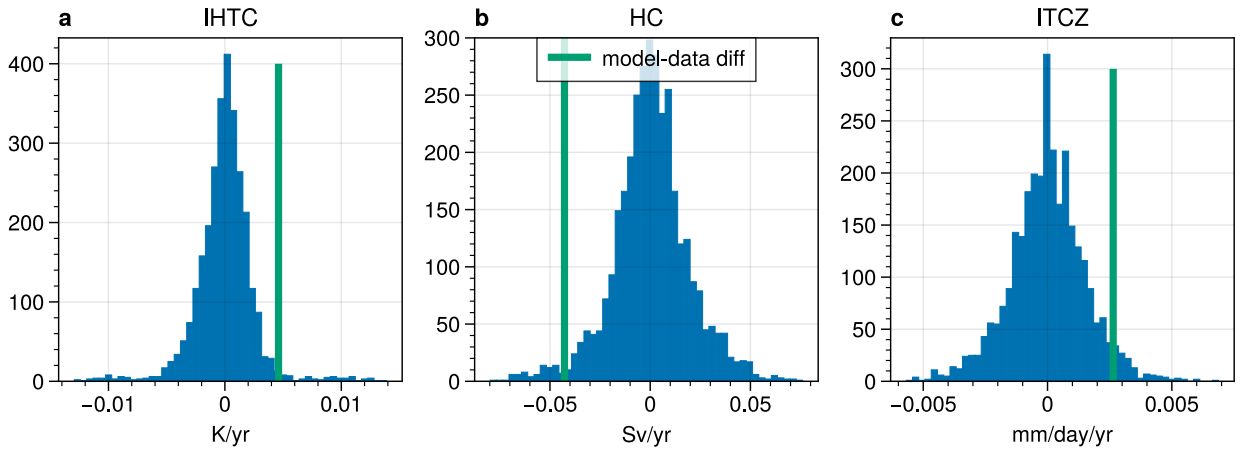

Extended Data Fig. 3 Comparison of model-data difference with modeled internal variability. a, IHTC. **b,** HC. **c,** ITCZ. We calculated distributions from 34 CMIP6 models with at least 200 years of preindustrial control simulations. To remove long-term drift, we detrended the entire time series for each model. Next, we randomly selected a continuous 65-year time series and calculated trends. This process was repeated 100 times for each model, resulting in a total of 3400 realizations. For the IHTC, 153 out of 3400 realizations (~4.5%) show a trend with an absolute value (two-tail) greater than the model-data difference. For the HC, 154 out of 3400 realizations (~4.5%) show a trend with an absolute value greater than the model-data difference. For the ITCZ, 261 out of 3400 realizations (~7.5%) show a trend with an absolute value greater than the model-data difference. Given the IHTC, HC, and ITCZ are a highly coupled system, only 51 out of 3400 realizations (~1.5%) show a trend with an absolute value greater than the model-data difference collectively.

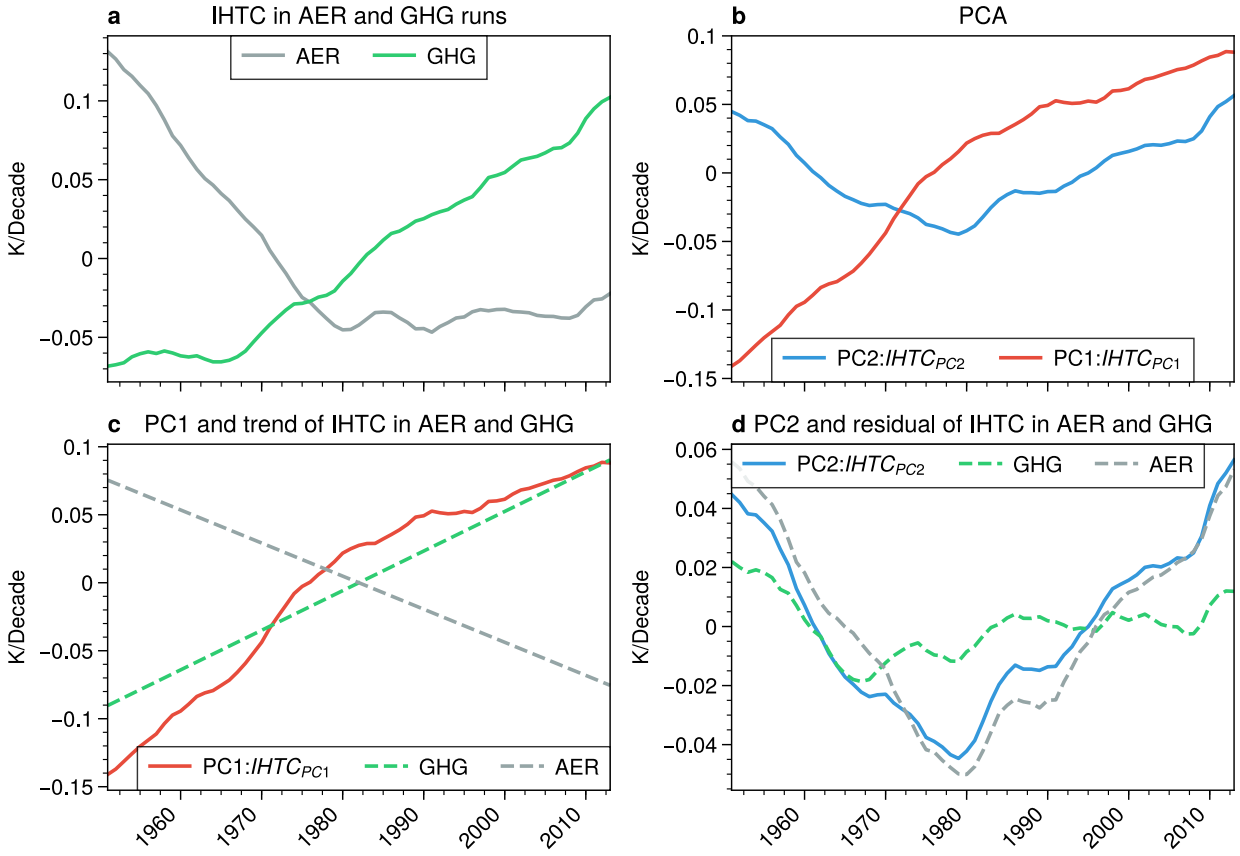

Extended Data Fig. 4 PCA on IHTCs in AER and GHG runs. a, forced IHTC due to AER and GHG. **b,** PCs of IHTC in **a**. **c,** PC1 and linear trend of the IHTC in AER and GHG. **d,** PC2 and detrended (or multidecadal) IHTC in AER and GHG. The loading has been normalized to unit variance, so the PC shown here has absolute unit.

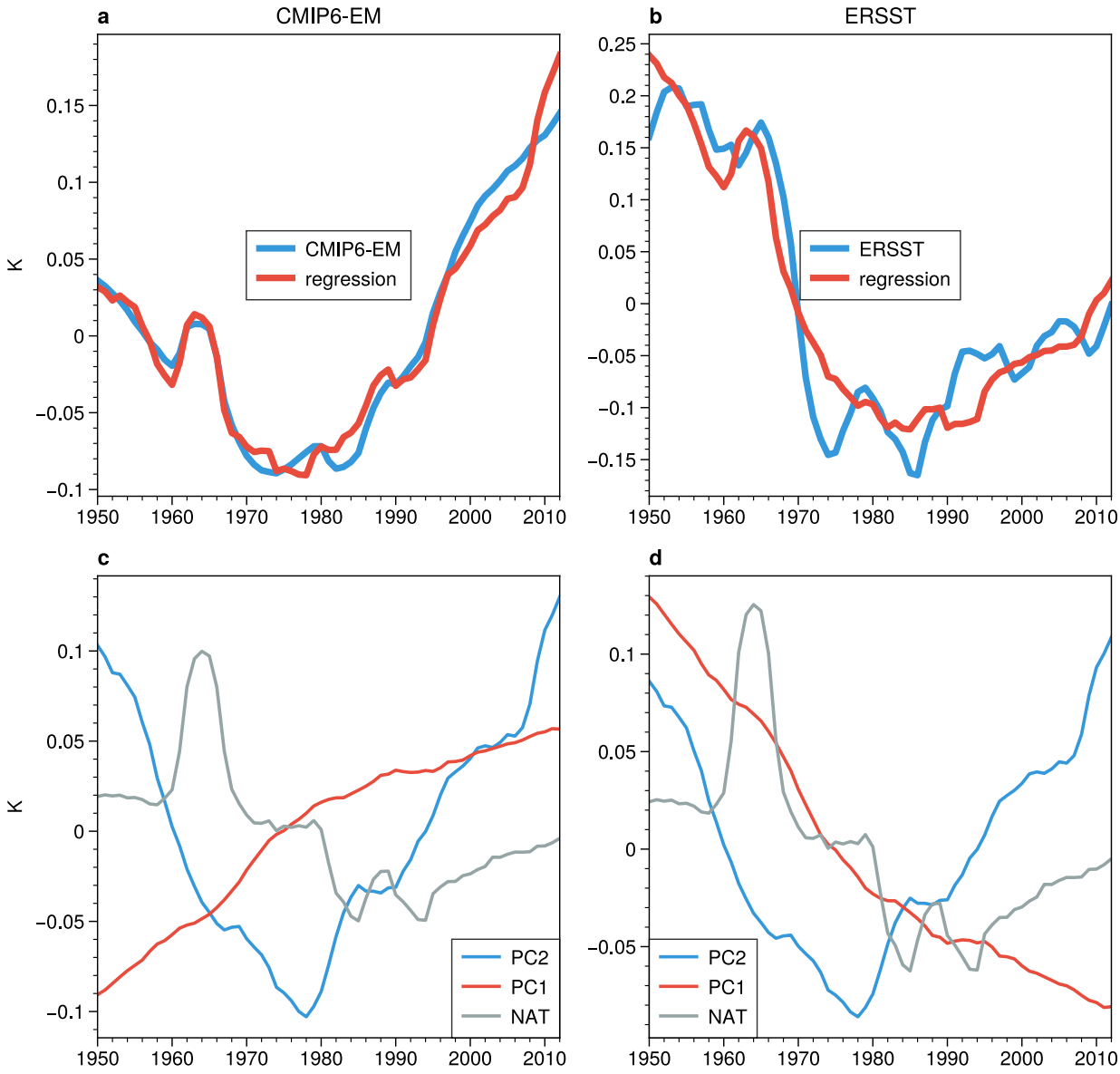

Extended Data Fig. 5 Decomposition of Equation 2. a, IHTC and its regression in the model. **b,** as in **a,** but for ERSSTv5. **c,** decomposition of the regression in the model. **d,** as in **c,** but for ERSSTv5.

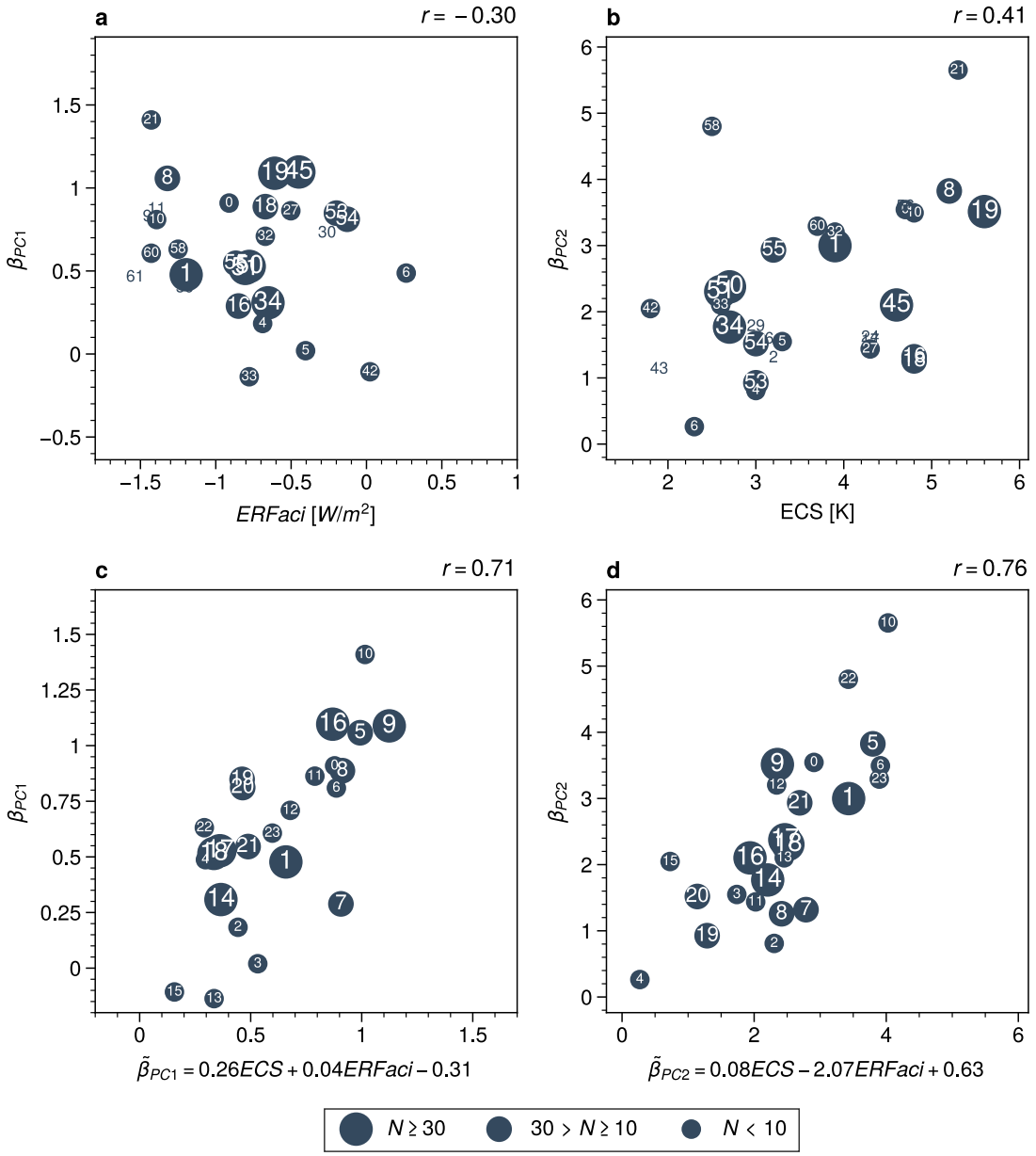

Extended Data Fig. 6 Relationship between long-term trends and multidecadal variability in CMIP6 models' IHTC with their responses to GHG and AER. a, scatterplot showing the relationship between β_{PC1} and ERFaci. **b,** scatterplot showing the relationship between β_{PC2} and ECS. **c,** scatterplot showing the relationship between β_{PC1} and regression of β_{PC1} onto ECS and ERFaci. **d,** scatterplot showing the relationship between β_{PC2} and regression of β_{PC2} onto ECS and ERFaci. Models are divided into two groups: those with ECS and ERFaci available (circled) and those with either ECS or ERFaci (non-circled). Circle sizes are proportional to each model's ensemble size (legend). Correlations in **a** and **b** are calculated using circled models, and they remain almost the same if including non-circled models.

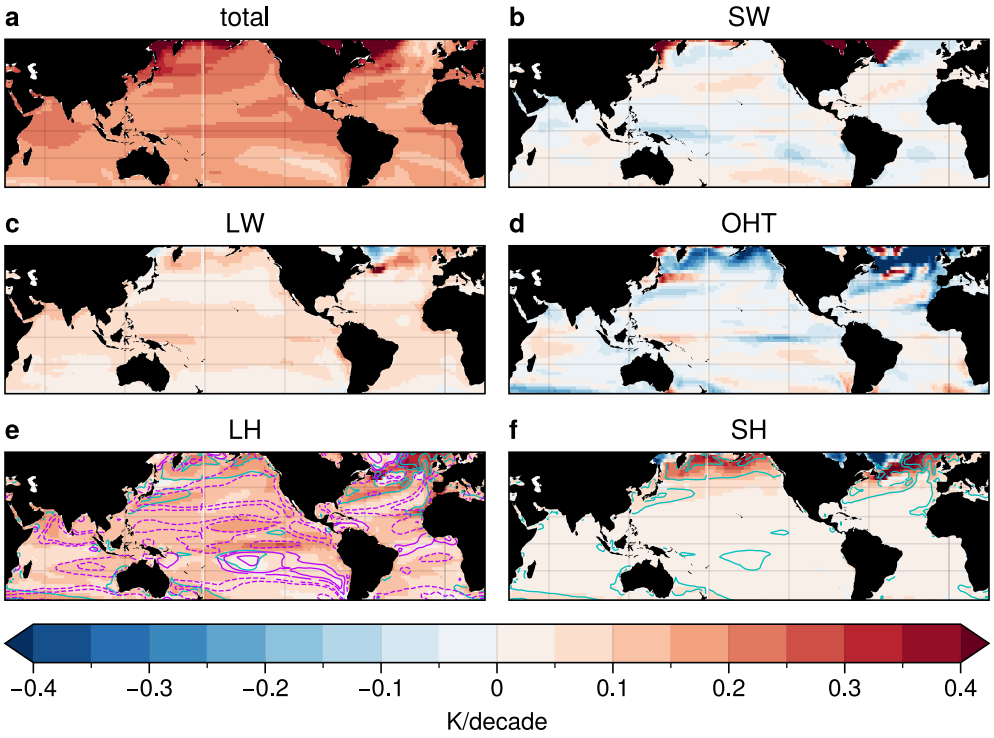

Extended Data Fig. 7 Energy budget analysis for the global SST trend during 1950-2014 in CMIP6 GHG run. a, total SST trend. **b,** SST trend due to changes in shortwave. **c, d, e,** and **f** as in **b** but for longwave, ocean dynamics, latent heat and sensible heat, respectively. The trend of the air-sea temperature difference is plotted in cyan contours in **e** and **f**. The surface wind speed trend is plotted in purple contours in **e**, with positive (negative) change in solid (dashed) line.

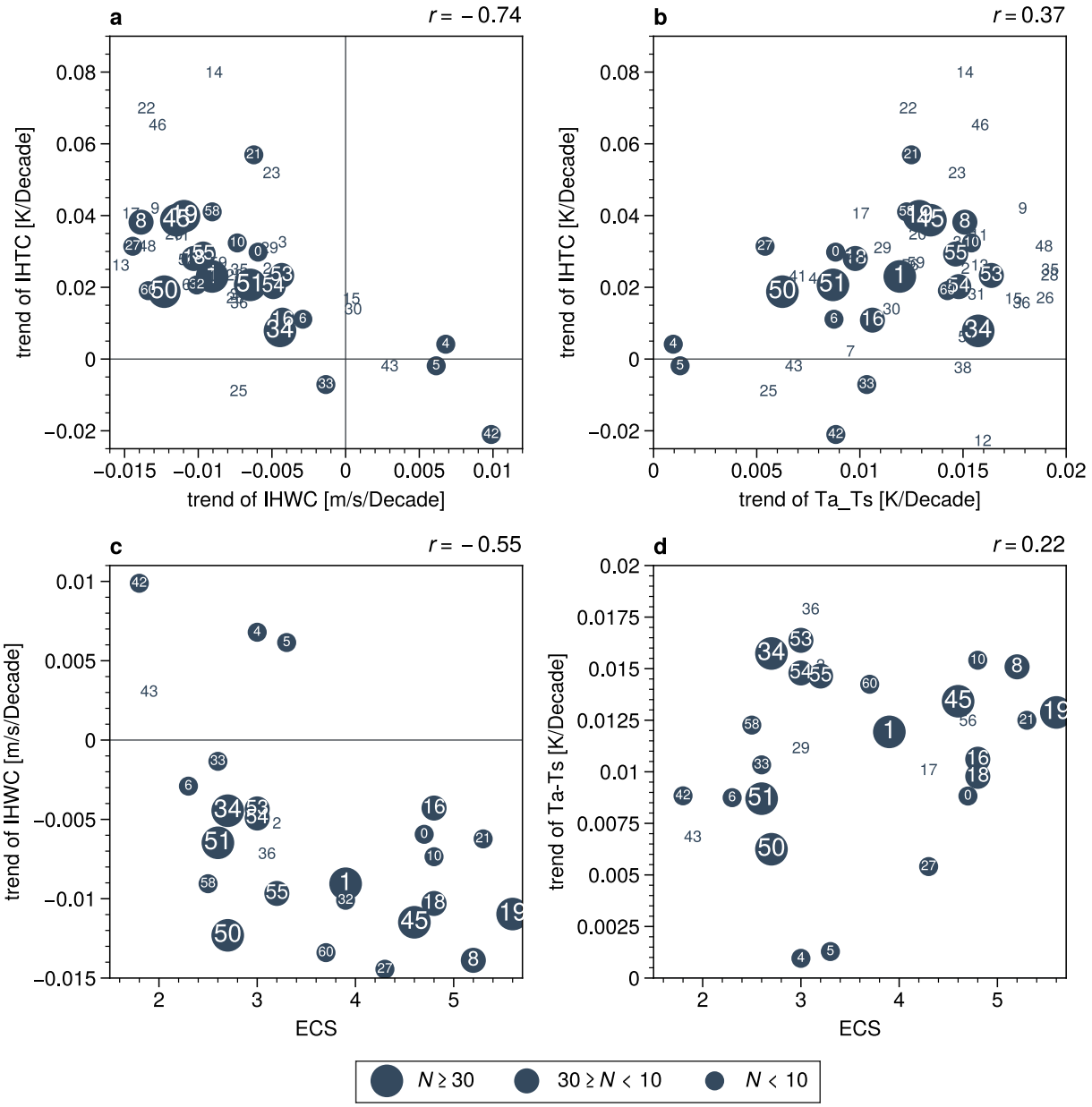

Extended Data Fig. 8 Scatterplot illustrating the relationship between IHTC, IHWC, air-sea temperature difference, and ECS in CMIP6 models. a, trends of IHTC and IHTC. **b,** trends of IHTC and air-sea temperature difference. **c,** ECS and trend of IHWC. **d,** ECS and trend of air-sea temperature difference. The trends are calculated in 1950-2014. The correlation shown in top-right corner is calculated using 24 models that have both ECS and ERFaci available. The correlation in **a** decreases slightly from -0.74 to -0.62, and in **b** it decreases from 0.37 to 0.27 when calculated using all models instead of just the circled ones. In **c** and **d**, the correlation remains almost the same when using all models.

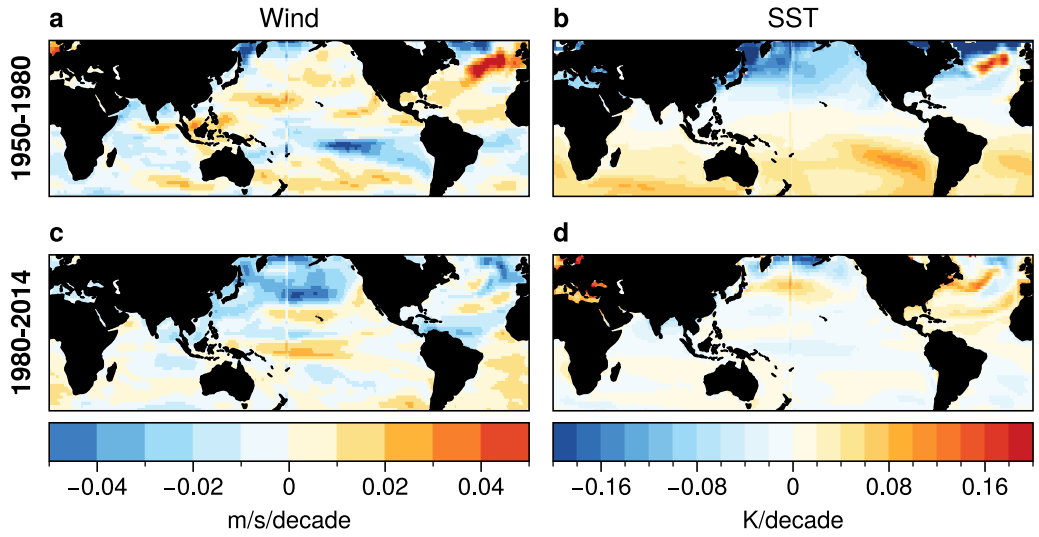

Extended Data Fig. 9 Linear trend of surface wind speed and SST in AER simulations. a, AER-induced surface wind speed trend in 1950-1980. **b,** as in **a** but for SST**. c, d** as in **a, b** but for 1980-2014. Note that in **b** and **d,** the global mean SST have been removed to emphasize the NH-SH gradient.

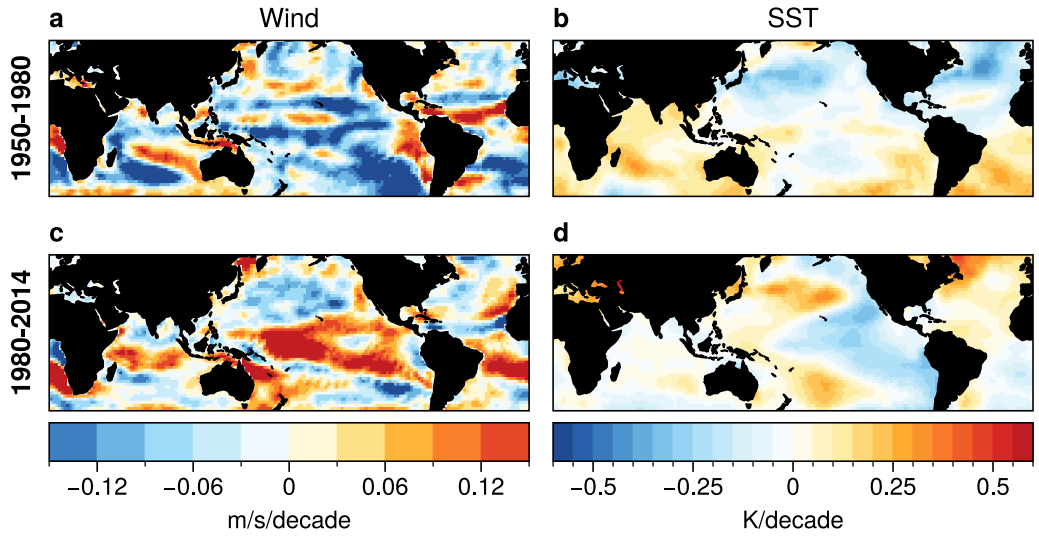

Extended Data Fig. 10, as in Extended Data Fig. 9, but for observation (ERSSTv5 and 20th century reanalysis).

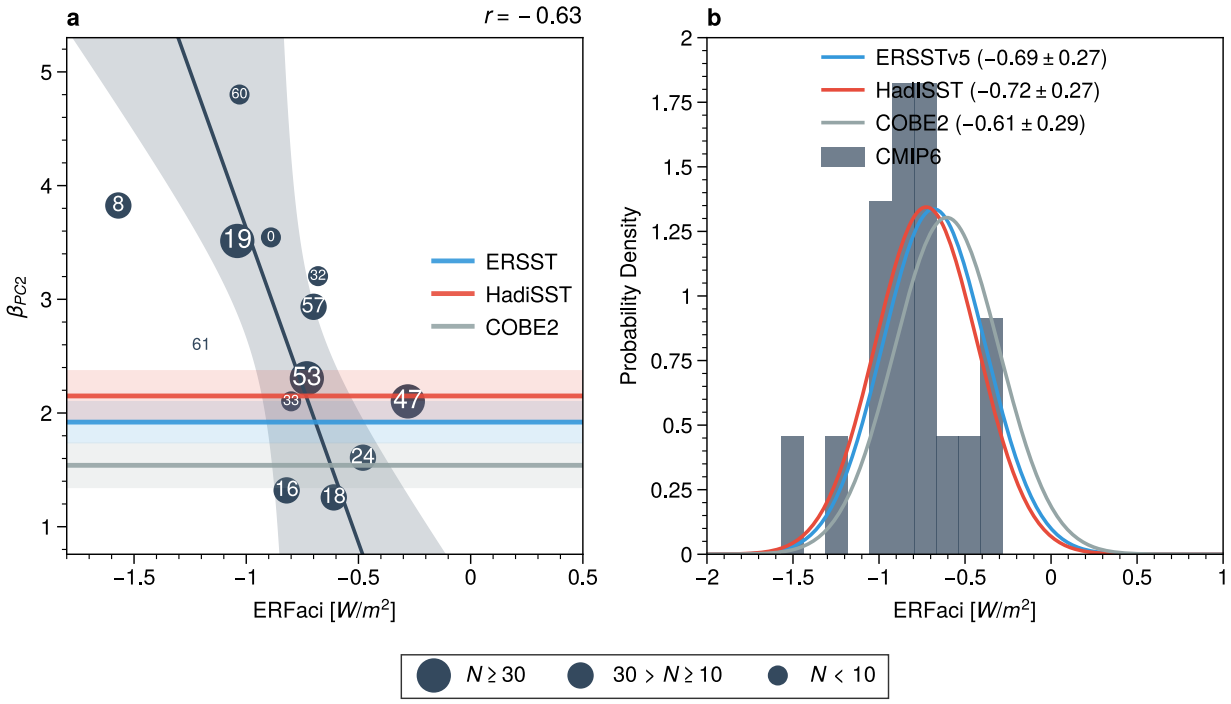

Extended Data Fig. 11 Emergent constraint on the ERFaci in real world. a, scatterplot between β_{PC2} and ERFaci. **b,** probability density function for ERFaci in both models and observations. In panel **a,** the solid dark line represents the best-fit linear regression of ERFaci on β_{PC2} across the model ensemble, with prediction error indicated by dark shadings. Horizontal lines denote the best-estimated β_{PC2} from various observations, with shading indicating one standard deviation.